

# Frozen Orbits at high eccentricity and inclination: Application to Mercury orbiter.

N. Delsate<sup>1</sup> · P. Robutel<sup>2</sup> · A. Lemaître<sup>1</sup> ·  
T. Carletti<sup>1</sup>

Received: date / Accepted: date

**Abstract** We hereby study the stability of a massless probe orbiting around an oblate central body (planet or planetary satellite) perturbed by a third body, assumed to lie in the equatorial plane (Sun or Jupiter for example) using an Hamiltonian formalism.

We are able to determine, in the parameters space, the location of the frozen orbits, namely orbits whose orbital elements remain constant on average, to characterize their stability/unstability and to compute the periods of the equilibria.

The proposed theory is general enough, to be applied to a wide range of probes around planet or natural planetary satellites.

The BepiColombo mission is used to motivate our analysis and to provide specific numerical data to check our analytical results.

Finally, we also bring to the light that the coefficient  $J_2$  is able to protect against the increasing of the eccentricity due to the Kozai-Lidov effect.

**Keywords** Methods: analytical study · Stability · Long-term evolution · Kozai resonances · Frozen Orbit equilibria

## 1 Introduction

BepiColombo (MPO and MMO orbiters) is a joint European and Japanese space agencies space mission aimed at studying the planet Mercury. The MPO (Mercury Planetary Orbiter) will be brought into a polar elliptical orbit around Mercury with an inclination of  $88-90^\circ$ , an eccentricity of 0.1632 and a semi-major axis of 3 394 km. The MMO (Mercury Magnetospheric Orbiter) will also be brought into a polar elliptical orbit with an eccentricity of 0.6679 and a semi-major axis of 8 552 km.

Actually polar orbits are very interesting for scientific missions to planetary satellites (with near polar low-altitude) or to planet (with high-eccentric high-altitude). The orbital dynamics of such space probes is governed by the oblateness ( $J_2$  effect) of the

<sup>1</sup> University of Namur, Department of Mathematics Rempart de la Vierge 8, B-5000 NAMUR, BELGIUM

E-mail: nicolas.delsate@math.fundp.ac.be

<sup>2</sup> IMCCE, CNRS UMR8028, Observatoire de Paris/USTL/UPMC, 77 Av. Denfert-Rochereau, F-75014 Paris, France.

central body around which the space probe is orbiting and the gravity field from the third body. A well-known effect of the third-body perturbation is the change in the stability of circular orbits related to orbit inclination. This effect is a natural consequence of the Kozai-Lidov resonance (Kozai 1962; Lidov 1963). The final fate of such a satellite is the collision with the central body. Therefore the control of the orbital eccentricity leads to the control of the satellite lifetime.

Scheeres et al (2001) studied near-circular orbits in a model that included both the third body’s gravity and  $J_2$ . In addition San-Juan et al (2006) studied orbit dynamics about oblate planetary satellites using a rigorous averaging method. Paskowitz and Scheeres (2006) added the effect of the coefficient  $J_3$ . These authors mainly focused their attention to an orbiter around planetary satellites especially for Europa orbiter. So they did not take into account the eccentricity of the third body and they detailed the near-circular orbits.

Our purpose is to build a simplified Hamiltonian model, as simple as possible, which will reproduce the motion of probes orbiting an oblate central body also taking into account the third body effect. Especially we are looking for the conditions that give rise to frozen orbits. Frozen orbits are orbits that have orbital elements constant on average. These particular orbits are able to keep constant the eccentricity. Therefore in a neighbourhood of these orbits there is a stability area where even a limited control could be used to avoid the crash onto the central body.

Beside the oblateness of the central body and the gravity effect of the third body, our averaged model takes into account also the eccentricity of the orbit of the third body. Moreover let us observe that our results are given in closed form with respect to eccentricity and inclination of the probe, namely we do not perform any power series expansion; therefore, our theory applies for arbitrary eccentricities and inclinations of the space probe, and is not limited to almost-circular orbits. We can thus conclude that the theory is general enough to be applied to a wide range of probes around a planet or around a natural planetary satellite and, can be formulated and presented in a general way that allows extension of the results to other cases.

The Mercury orbiter mission (BepiColombo) is used to motivate our analysis and to provide specific numerical data to check our analytical results.

We are able to provide the location of frozen orbits and study their stability as a function of the involved parameters, using implicit equations and graphics. Finally we give the analytical expressions of the periods at the stable equilibria.

The analytical results are verified and confirmed using dedicated numerical simulations of the whole model.

To conclude, we discuss the effect of the protection of  $J_2$  on the increase of the eccentricity due to Kozai-Lidov effect and the apparition of an asymmetry caused by the addition of the coefficient  $J_3$ .

## 2 Motivation: numerical exploration

For the purpose of our study, we consider the modeling of a space probe subjected to the influence of Mercury’s gravity field (in the following sections Mercury will be denoted by “central body”) and the gravitational perturbations of the Sun (noted “third body”) as well as to the direct solar radiation pressure without shadowing effect. As a consequence the differential system of equations is given by

$$\ddot{\mathbf{r}} = \ddot{\mathbf{r}}_{\text{pot}} + \ddot{\mathbf{r}}_{\odot} + \ddot{\mathbf{r}}_{\text{rp}}, \quad (1)$$

where  $\ddot{\mathbf{r}}_{\text{pot}}$  is the acceleration induced by Mercury’s gravity field,  $\ddot{\mathbf{r}}_{\odot}$  is the acceleration resulting from the gravity interaction with the Sun and  $\ddot{\mathbf{r}}_{rp}$  is the acceleration due to the direct solar radiation pressure.

It is worth noting that we modelise the gravity potential of central body only using the  $J_2$ ,  $C_{22}$  and  $J_3$  coefficients. In our implementation, we choose the high accurate Solar System ephemeris given by the Jet Propulsion Laboratory (JPL) to provide the positions of the Sun (Standish 1998). We adopt the variable step size Bulirsch-Stoer algorithm (see e.g. Stoer and Bulirsch 1980) to numerically integrate the differential equation (1). Let us note that, for the purpose of validation, we also use a second numerical integrator DOP853 (an explicit Runge-Kutta method of order 8(5,3) with stepsize control due to Dormand & Prince (Hairer et al 1993)).

In Figure 1 we report the results of a numerical integration of the system of equations (1) for a set of 19600 orbits, propagated over a 200 years time span with a entry-level step size of 300 seconds. We consider a set of initial conditions defined by an eccentricity grid of 0.005 and a semi-major axis grid of 35 km, spanning the [2600, 7600] km range. The other fixed initial conditions are  $i_0 = 90^\circ$  for the inclination,  $\Omega_0 = 67.7^\circ$   $\omega_0 = -2^\circ$  for the longitude of the ascending node and the argument of periherm, respectively;  $M_0 = 36.4^\circ$  the mean anomaly at epoch fixed at 14 September 2019. The area-to-mass ratio  $A/m = 0.01\text{m}^2/\text{kg}$ . These values have been fixed by the initial conditions of BepiColombo mission found in Garcia et al (2007).

We show the amplitude of the eccentricity (that is the difference between the maximum and minimum eccentricity reached during the integration) of each orbit in the left panel of Figure 1. For each orbit, we also calculate using the Numerical Analysis of Fundamental Frequencies, for short NAFF (Laskar 1988, 2005), the fundamental frequency (noted  $\nu$ ) of the evolution of the eccentricity vector ( $e \cos \omega, e \sin \omega$ ). We plot the logarithm of the second derivative (noted  $\log(\delta\delta\nu)$ ) of this frequency in the right panel of Figure 1, namely an indicator of the diffusion in the frequency space, hence the regularity of the orbit. For more details concerning this use of frequency analysis, see Lemaître et al (2009) where the frequency analysis has been used to study resonances in Geostationary Earth Orbits.

First, let us observe that the white zone in Figure 1 corresponds to orbits that crash onto central body’s surface. Second we distinguish a curve where the variation of the eccentricity amplitude is null (dashed black line). On the second derivative plot (right panel) we also distinguish on the left of the dashed black line (null-variation of eccentricity) a larger value of the log of the derivative that could correspond to a separatrix.

These structures will be analyzed and explained using a simplified model, that takes into account the central body attraction with the  $J_2$  harmonic coefficient and the third body gravitational effect. We observed that the solar radiation pressure does not play any role in these structures, hence this effect will be absent in the simplified model.

### 3 The Hamiltonian Formalism

The aim of this section is to introduce the Hamiltonian (2) already found in Tremaine et al (2009). Kepler’s Hamiltonian describing the motion of a test particule orbiting an isolated point mass M is

$$\mathcal{H}_K = \frac{1}{2}v^2 - \frac{GM}{r} = \frac{GM}{a}$$

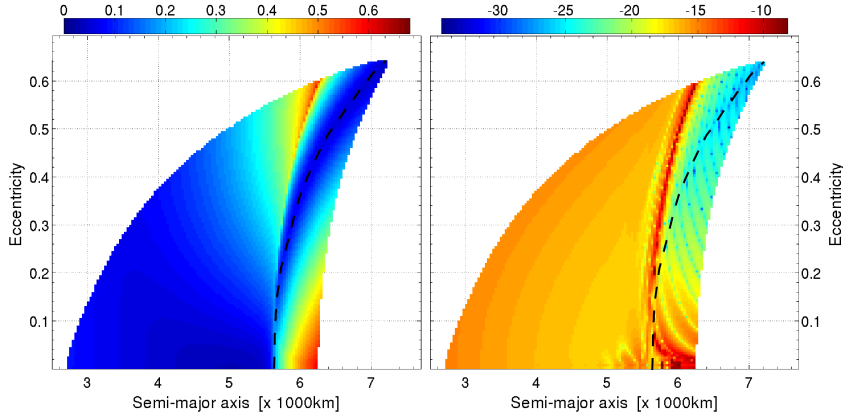


**Fig. 1** The eccentricity computed as a function of the initial eccentricity  $e_0$  and the initial semi-major axis  $a_0$ . The equations of motion include the central body attraction, the harmonics  $J_2, C_{22}, J_3$ , the solar interaction as well as the perturbing effects of the solar radiation pressure ( $A/m = 0.01\text{m}^2/\text{kg}$ ). The eccentricity step is 0.005 and the semi-major axis step is 35 km. The initial conditions are  $i_0 = 90^\circ, \Omega_0 = 67.7^\circ, \omega_0 = -2^\circ$  and  $M_0 = 36.4^\circ$ . The integration time is 200 years from epoch fixed at 14 September 2019. The patterns have been obtained by plotting the amplitude of variation of the eccentricity and  $\log(\delta\delta\nu)$  respectively in left and right panel.

where  $G$  is the gravitational constant,  $\mathbf{r}$  is the planetocentric position of the particule,  $\mathbf{v} = \dot{\mathbf{r}}$ ,  $r = |\mathbf{r}|$  and  $a$  is the semi-major axis of the particule.

One can introduce the quadrupole potential arising from an oblate planet (“central body”) that is

$$\Phi_{J_2}(\mathbf{r}) = \frac{GMJ_2R_p^2}{2r^5} \left[ 3(\mathbf{r} \cdot \mathbf{n}_p)^2 - r^2 \right]$$

where  $\mathbf{n}_p$  is the unit vector oriented to central body’s spin axis (see Figure 2).  $M$ ,  $R_p$  and  $J_2$  are respectively the mass, the radius and the oblateness coefficient of the central body (planet or natural satellite).

We assume that  $r \ll a_{3b}$  (where the subscript  $3b$  is related to the third body) and we average over the third body orbital period. So, we obtain the quadrupole in terms of the third body gravitational effect

$$\Phi_{3b}(\mathbf{r}) = \frac{GM_{3b}}{4a_{3b}^3(1 - e_{3b}^2)^{3/2}} \left[ 3(\mathbf{r} \cdot \mathbf{n}_{3b})^2 - r^2 \right]$$

where  $\mathbf{n}_{3b}$  is the normal to the central body orbit.  $M_{3b}$ ,  $a_{3b}$  and  $e_{3b}$  are respectively the mass, the semi-major axis and the eccentricity of the third body. This quadrupole term takes into account the eccentricity ( $e_{3b}$ ) of the third body (e.g. Sun or Jupiter) around the central body (planet or natural satellite). Let us stress the fact that Paskowitz and Scheeres (2004); San-Juan et al (2006); Scheeres et al (2001) do not include this eccentricity factor in their formulation, while for a Sun-Mercury-orbiter application, this will be an important contribution.

We then average over the Keplerian orbit of the test particule described by the following elements: a semi-major axis  $a$ , an eccentricity  $e$ , and an orientation specified

by the unit vectors  $\mathbf{n}$  along the angular momentum vector,  $\mathbf{u}$  toward the pericenter and  $\mathbf{v} = \mathbf{n} \times \mathbf{u}$ . We have (Brouwer and Clemence 1961)

$$\begin{aligned} \langle r^2 \rangle &= a^2 \left(1 + \frac{3}{2}e^2\right), & \left\langle \frac{1}{r^3} \right\rangle &= \frac{1}{a^3(1-e^2)^{3/2}}, \\ \langle (\mathbf{r} \cdot \mathbf{u})^2 \rangle &= a^2 \left(\frac{1}{2} + 2e^2\right), & \langle (\mathbf{r} \cdot \mathbf{v})^2 \rangle &= a^2 \left(\frac{1}{2} - \frac{1}{2}e^2\right), \\ \left\langle \frac{(\mathbf{r} \cdot \mathbf{u})^2}{r^5} \right\rangle &= \left\langle \frac{(\mathbf{r} \cdot \mathbf{v})^2}{r^5} \right\rangle = \frac{1}{2a^3(1-e^2)^{3/2}}. \end{aligned}$$

where  $\langle \rangle$  denotes the average over  $M$ , the mean anomaly of the orbit.

Let  $\mathbf{j} \equiv \sqrt{1-e^2} \mathbf{n}$ ,  $\mathbf{e} = e\mathbf{u}$ ,  $\tau = \sqrt{\frac{GM}{a^3}}t$ ,  $\varepsilon_{J_2} = \frac{J_2 R_p^2}{a^2}$  and  $\varepsilon_{3b} = \frac{M_{3b} a^3}{M a_{3b}^3 (1-e_{3b}^2)^{3/2}}$  where  $\mathbf{e}$  is the eccentricity vector and  $\varepsilon_{J_2} \geq 0$ ,  $\varepsilon_{3b} \geq 0$ . We finally define a dimensionless (divided by  $GM/a$ ) Hamiltonian

$$\mathcal{K}' = -\frac{1}{2} + \frac{\varepsilon_{J_2}}{4(1-e^2)^{5/2}} \left[1 - e^2 - 3(\mathbf{j} \cdot \mathbf{n}_p)^2\right] + \frac{3\varepsilon_{3b}}{8} \left[5(\mathbf{e} \cdot \mathbf{n}_{3b})^2 - (\mathbf{j} \cdot \mathbf{n}_{3b})^2 - 2e^2\right], \quad (2)$$

That describes the secular equations of motion of a test particule around an oblate central body perturbed by the third body gravitational effect. Let us summarize the used assumptions:

1. the precession rate of the central body spin due to third body gravity is negligible;
2. the satellite is a massless test particule;
3. the third body is far enough from the central body such that the third body gravity can be approximated by a quadrupole;
4. the satellite is far enough from the central body so that the potential from the central body can be approximated as a monopole plus a quadrupole;
5. the perturbing forces ( $\Phi_{J_2} + \Phi_{3b}$ ) are weak enough so that the secular equations of motion can be used to describe the orbital motion;
6. there are not resonant relations in mean motions between the frequencies of the satellite and the frequencies of the central body.

Let us remark that San-Juan et al (2006) already studied the orbit dynamics about planetary satellites using an extensive averaging method based on the Lie transforms to obtain averaged equations involving higher orders whose result is the introduction of an asymmetry for direct and retrograde satellite. Our simplified model will not be able to capture this asymmetry because the resulting Hamiltonian (3) will be symmetric in the satellite inclination; thus direct and retrograde satellites will have the same behavior.

Let us now make some assumptions suitable in the case of a non-inclined central body orbit (e.g. Sun-Mercury-orbiter system or Jupiter-Europa-orbiter system). We hereby consider an equatorial third body, thus  $\mathbf{n}_p = \mathbf{n}_{3b}$ . We also set  $G = \sqrt{1-e^2}$  and  $H = G \cos \iota$  where  $\mathbf{j} \cdot \mathbf{n}_p = \sqrt{1-e^2} \cos \iota$ . To eliminate an extra parameter, we divide the Hamiltonian by the coefficient  $\varepsilon_{J_2}$  and we introduce the coefficient  $\gamma$

$$\gamma = \frac{\varepsilon_{3b}}{\varepsilon_{J_2}} = \frac{M_{3b}}{M a_{3b}^3 (1-e_{3b}^2)^{3/2}} \frac{a^5}{J_2 R_p^2}.$$

In Figure 2, we represent the geometry for the general problem (on the left) and for our simplified one (on the right).

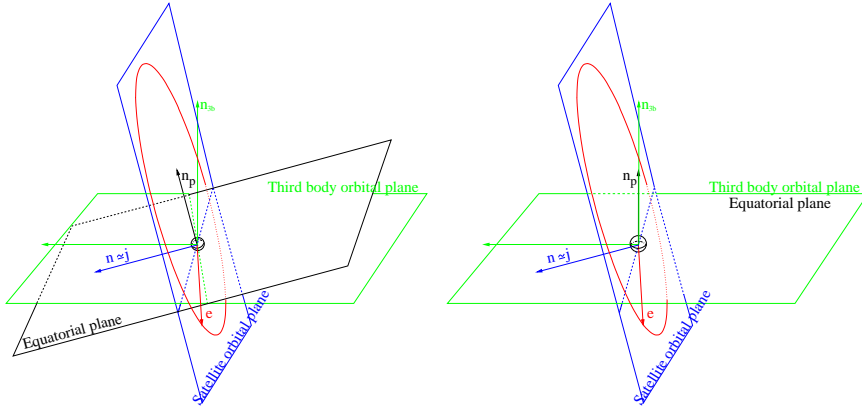


**Fig. 2** Reference planes, for the general theory on the left and for our particular case on the right.

The averaged Hamiltonian is then

$$\left\{ \begin{array}{l} \mathcal{K}' = \frac{\varepsilon_{J_2}}{4G^3} \left( 1 - 3\frac{H^2}{G^2} \right) + \frac{3\varepsilon_{3b}}{8} \left[ 5(1 - G^2) \left( 1 - \frac{H^2}{G^2} \right) \sin^2 \omega - H^2 - 2 + 2G^2 \right] \\ \xleftrightarrow[\text{noted by } \mathcal{K}]{\mathcal{K}' / \varepsilon_{J_2}} \mathcal{K} = \frac{1}{4G^3} \left( 1 - 3\frac{H^2}{G^2} \right) + \frac{3\gamma}{8} \left[ 5(1 - G^2) \left( 1 - \frac{H^2}{G^2} \right) \sin^2 \omega - H^2 - 2 + 2G^2 \right]. \end{array} \right. \quad (3)$$

This Hamiltonian is independent of the ascending node  $\Omega$ . If we take  $\gamma = 0$  ( $\varepsilon_{3b} = 0$ , namely we take into account only the oblateness effect), we have the well-known circular dynamics of the eccentricity vector due to the  $J_2$  coefficient with an elliptical fixed point in the semi-equinoctial elements  $(k, h) = (\sqrt{1 - G^2} \cos \omega, \sqrt{1 - G^2} \sin \omega)$ . If we take  $\gamma \rightarrow \infty$  ( $\varepsilon_{J_2} = 0$  i.e. only the third body contribution does matter), we find the Kozai-Lidov Hamiltonian which we find in a similar formalism in Paskowitz and Scheeres (2004) (with  $e_{3b} = 0$ ). The Hamiltonian (3) (with  $e_{3b} = 0$ ) can also be found in Scheeres et al (2001).

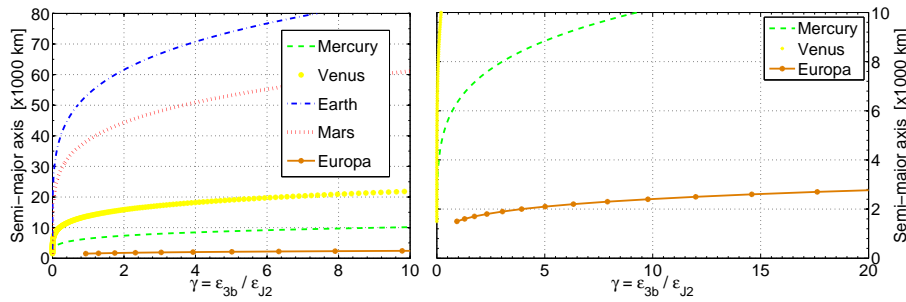


**Fig. 3** Relation between  $\gamma$  and the semi-major axis of a test particule orbiting the central body (terrestrial planets or Europa). The third body are respectively the Sun and Jupiter.

**Table 1** Connection between semi-major axis (km) of the probe around the central body and the coefficient  $\gamma$ . The rows “Min.,” “Missions” and “Hill” give the values of  $\gamma$  with respect to the semi-major axis respectively equal to the radius of the central body, to one space mission and to the radius of the Hill’s sphere. The “-” symbol indicates that the semi-major axis is lower than the radius of the central body or greater than the radius of the Hill’s sphere.

		Min.	Missions	Hill	Particular values	
Mercury	$a$ (km)	2 439.990	Messenger 10 136.2	175 295	4 350	5 577
	$\gamma$	0.008	9.9136	$1.533 \times 10^7$	1/7	0.5
Venus	$a$ (km)	6 051.8	Venus Express 39 176.8	1 004 270	9 350	12 010
	$\gamma$	0.008	184.485	$2.042 \times 10^9$	1/7	0.5
Earth	$a$ (km)	6 378.137	Meteosat 42 164.14	1 471 506	36 350	46 670
	$\gamma$	$2.38 \times 10^{-5}$	0.30107	$1.559 \times 10^7$	1/7	0.5
Mars	$a$ (km)	3 396.190	Mars Express 9 311.95	982 748	26 150	33 580
	$\gamma$	$5.288 \times 10^{-6}$	$8.195 \times 10^{-4}$	$1.073 \times 10^7$	1/7	0.5
Europa	$a$ (km)	1 565.0	EJSM/JEO 3 222	13 529	-	-
	$\gamma$	1.153	42.646	$5.568 \times 10^4$	1/7	0.5

For illustration, we respectively show in the Table 1 and draw in Figure 3 the value of the coefficient  $\gamma$  with respect to the semi-major axis for a probe around a terrestrial planet and around Europa. This coefficient can be related to other parameters used in the literature. For example, it can be linked to the coefficient  $\beta$  in San-Juan et al (2006) or to the coefficient  $\epsilon$  used in Scheeres et al (2001).

#### 4 Secular Equations of Motion

From the doubly averaged Hamiltonian (3), we obtain the equations of motion:

$$\dot{\Omega} = -H \left\{ \frac{3}{2G^5} + \frac{3\gamma}{8} \left[ \frac{10}{G^2} (1 - G^2) \sin^2 \omega + 2 \right] \right\} \quad (4)$$

$$\begin{aligned} \dot{H} &= 0 \\ \dot{\omega} &= \frac{3\gamma}{4} \left[ 5 \left( \frac{H^2}{G^3} - G \right) \sin^2 \omega + 2G \right] + \frac{3}{4G^4} \left( 5 \frac{H^2}{G^2} - 1 \right) \end{aligned} \quad (5)$$

$$\dot{G} = -\frac{15\gamma}{4} (1 - G^2) \left( 1 - \frac{H^2}{G^2} \right) \sin \omega \cos \omega . \quad (6)$$

Developing these equations in eccentricity up to second order, we can obtain the equations of Scheeres et al (2001). In the following, we will adopt a complementary approach, keeping functions of eccentricity and inclination, without power series developments, in such a way that our results hold for any arbitrary eccentricities and inclinations.

From the previous set of equations, we observe that  $H$  is a constant of motion, and  $H^2 = G^2 \cos^2 i$  too, as in the Kozai-Lidov effect (Kozai 1962; Lidov 1963). Besides, let us remark that  $0 \leq G \leq 1$ , thus  $0 \leq H \leq G \leq 1$  and moreover  $\gamma > 0$ . The first equation (4) is equal to zero only for  $H = 0$  corresponding to exact polar inclination. Moreover the ascending node does not affect any of the other orbital elements. The last equation

(6) equals to zero for  $G = 1$ ,  $\omega = k\pi/2$ ,  $k \in \mathbb{N}$  or  $H = G$ , namely  $i = 0^\circ$ , that is the planar case. The third equation (5) could equal to zero for  $\omega = 0, \pi$  or  $\omega = \pm\pi/2$ . We analyze these equations in next section to find the equilibria.

## 5 Frozen Orbit Solutions

A frozen orbit is characterized by no secular change in orbital eccentricity and argument of pericenter. It has constant values of  $e$ ,  $i$  and  $\omega$  on average, this results in fixed geometrical size and locations, apart from short period oscillations.

We already observed that equilibria appear when  $G = 1$  or  $\omega = 0, \pi$  or  $\omega = \pm\pi/2$ . We separately deal with these three different cases. For each of them, we give the number of equilibria, the conditions of existence and we calculate their stability.

We do not deal with the singularity  $G = 0$  ( $\Leftrightarrow e = 1$ ) because it corresponds to an escape of the orbiter. We will show that the equilibrium  $G = 1$  always exists. So to begin, we deal with the non-circular case  $G \neq 1$  (eccentricity  $\neq 0$ ).

### 5.1 Non-circular case $G \neq 1$ (eccentricity $\neq 0$ )

#### 5.1.1 Vertical equilibria – Kozai-Lidov equilibria: $\cos \omega = 0 \Leftrightarrow \omega = \pm\pi/2$

The conditions to simultaneously equal to zero the equations (5) and (6) is:

$$\begin{cases} H^2 = \frac{G^2}{5} \frac{1 + 3G^5\gamma}{1 + G^3\gamma} \\ \cos \omega = 0 \end{cases} \quad (7)$$

Because  $0 \leq G < 1$  then this equation implies that

$$H^2 < \frac{1 + 3\gamma}{5\gamma + 5}. \quad (8)$$

Let us observe that this is also the value for which one real root does exist. If this condition is violated then no real root exists.

Actually we determine a region given by the implicit equation

$$\begin{cases} 864\,000 H^{16} \gamma^6 + (2\,963\,520 H^{12} - 1\,024 H^{10}) \gamma^4 \\ \quad + (1\,512\,630 H^8 - 13\,965 H^6 - 22\,235\,661 H^{10}) \gamma^2 + 12 = 0 \\ \text{and } H^2 \leq \frac{1}{3087} \end{cases}$$

where it is possible to find three real roots. We will show that these three real roots appear for eccentricities larger than 0.996 59. Being a case close to an escape of the orbiter, we will leave to section 7.3.3 a discussion of this “local deformation”.

If the oblateness term is neglected ( $\varepsilon_{J_2} \simeq 0 \Leftrightarrow \gamma \rightarrow \infty$ ), the existence condition becomes independent of the physical parameter and reduces to  $\sin^2 i < \frac{2}{5}$  or  $\arccos \sqrt{\frac{3}{5}} \simeq 39.23^\circ \leq i \leq 144.77^\circ$  which corresponds to Kozai-Lidov critical inclination.



We also analyze the stability of these equilibria (7). The Jacobian of the Hamiltonian (3) evaluated at the equilibrium (7) (noted by  $|\text{Eq.}(7)$  or  $G_{kl}$  being the value of  $G$  at the Kozai-Lidov equilibrium) is given by:

$$\left\{ \begin{array}{l} \frac{\partial^2 \mathcal{K}}{\partial G^2} \Big|_{\text{Eq.}(7)} = \frac{3}{2G^5} \left( 2 - 15 \frac{H^2}{G^2} \right) - \frac{9\gamma}{4} \left( 1 + 5 \frac{H^2}{G^4} \right) \Big|_{\text{Eq.}(7)} \\ \qquad \qquad \qquad = \frac{3}{4G_{kl}^5} \frac{1}{1 + \gamma G_{kl}^3} \left( -2 + \gamma G_{kl}^3 - 21\gamma G_{kl}^5 - 12\gamma^2 G_{kl}^8 \right) \\ \frac{\partial^2 \mathcal{K}}{\partial \omega^2} \Big|_{\text{Eq.}(7)} = -\frac{15}{4} \gamma (1 - G^2) \left( 1 - \frac{H^2}{G^2} \right) \Big|_{\text{Eq.}(7)} \\ \qquad \qquad \qquad = -\frac{3}{2} \gamma (1 - G_{kl}^2) \left( \frac{2 - G_{kl}^5 \gamma}{1 + G_{kl}^3 \gamma} \right) \\ \frac{\partial^2 \mathcal{K}}{\partial G \partial \omega} \Big|_{\text{Eq.}(7)} = \frac{\partial^2 \mathcal{K}}{\partial \omega \partial G} \Big|_{\text{Eq.}(7)} = 0. \end{array} \right. \quad (9)$$

In the equations (9), the term  $\frac{\partial^2 \mathcal{K}}{\partial \omega^2} \Big|_{\text{Eq.}(7)}$  is always strictly negative (if  $G < 1$ ). Then the equilibrium is a stable point if

$$\frac{1}{G^5} \left( 2 - 15 \frac{H^2}{G^2} \right) - \frac{3\gamma}{2} \left( 1 + 5 \frac{H^2}{G^4} \right) \Big|_{\text{Eq.}(7)} < 0 \iff -2 - 21\gamma G_{kl}^5 + 15\gamma G_{kl} H^2 < 0. \quad (10)$$

This equation (10) is always satisfied for all  $\gamma > 0$ ,  $H^2 < \frac{1+3\gamma}{5\gamma+5}$  and  $G_{kl} < 1$  ( $e_{kl} > 0$ ). Therefore, for these conditions, we have two opposite stable points at  $\omega = \pm\pi/2$  and  $G$  such that  $H^2 = \frac{G^2}{5} \frac{1+3G^5\gamma}{1+G^3\gamma}$ .

For the inclination  $i = 90^\circ$  ( $H^2 = 0$ ) the equilibrium exists for the particular value of  $G = 0$  ( $e = 1$ ). This case is only theoretical and should not be considered, because it would correspond to an escape of the orbiter. In Figure 4 we give the location of the equilibria  $G$  (7) in the parameter space  $(\gamma, H^2)$ .

### 5.1.2 Horizontal equilibria: $\sin \omega = 0 \iff \omega = 0, \pi$

The conditions to simultaneously equal to zero the equations (5) and (6) are:

$$\left\{ \begin{array}{l} H^2 = \frac{G^2}{5} (1 - 2G^5\gamma) \\ \sin \omega = 0. \end{array} \right. \quad (11)$$

Using “*Le théorème d’algèbre de Sturm*” (Sturm 1835) (for more explanation see the Appendix) we calculate the number of roots ( $G$ ) in the range  $0 \leq G < 1$  of the equation (11) as a function of the parameters  $\gamma$  and  $H^2$ . For  $\gamma > 0$  this equation has

- one real root, equal to 0 if  $H^2 = 0$  and  $\gamma < 1/2$ .
- three real roots (one equal to 0 and the other two opposite) if  $H^2 = 0$  and  $\gamma \geq 1/2$ .
- three real roots (one equal to 1 and the other two opposite) if  $0 < H^2 < \frac{1-2\gamma}{5}$ ;
- five real roots (one equal to 1 and the other ones opposite two by two) if  $\gamma \geq 1/7$  and  $\frac{1-2\gamma}{5} < H^2 < \frac{(7\gamma)^{-2/5}}{7}$ ;
- one real root equal to 1 otherwise.

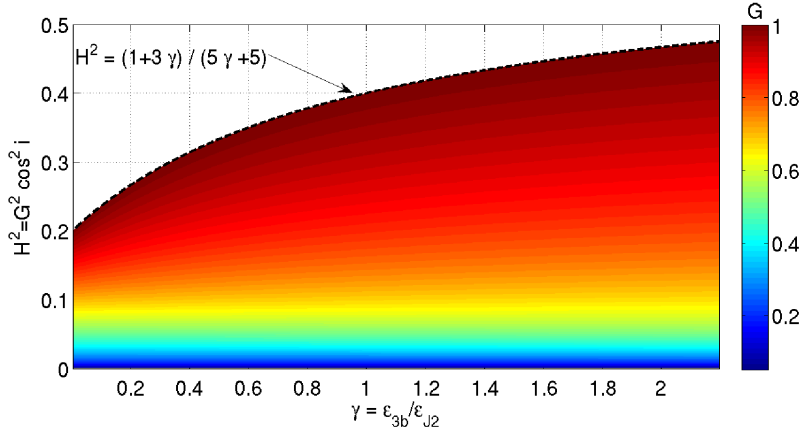


**Fig. 4** Values of  $G$  at Kozai-Lidov stable (Eqs. 7 and 8) equilibria (vertical equilibria:  $\omega = \pm\pi/2$ ) computed as a function of  $H^2$  and  $\gamma$ . These equilibria are always stable. The color code indicates the value of  $G$  at the equilibrium.

In Figure 5, we give the location of the equilibria  $G$  (11) in the space  $(\gamma, H^2)$ . The particular case  $G = 1$  will be treated in the next section. We can also analyze the stability of these equilibria (11). The Jacobian of the Hamiltonian (3) evaluated at the equilibrium (11) (noted by  $|_{\text{Eq.(11)}}$  or  $G_{hor}$ , being  $G_{hor}$  the value of  $G$  at the equilibrium) is given by:

$$\left\{ \begin{array}{l} \frac{\partial^2 \mathcal{K}}{\partial G^2} \Big|_{\text{Eq.(11)}} = \frac{3}{2G^5} \left( 2 - 15 \frac{H^2}{G^2} \right) + \frac{3\gamma}{2} \Big|_{\text{Eq.(11)}} \\ \qquad \qquad \qquad = \frac{3}{2G_{hor}^5} \left( -1 + 7\gamma G_{hor}^5 \right) \\ \frac{\partial^2 \mathcal{K}}{\partial \omega^2} \Big|_{\text{Eq.(11)}} = \frac{15}{4} \gamma (1 - G^2) \left( 1 - \frac{H^2}{G^2} \right) \Big|_{\text{Eq.(11)}} \\ \qquad \qquad \qquad = \frac{3}{2} \gamma (1 - G_{hor}^2) (2 + G_{hor}^5 \gamma) \\ \frac{\partial^2 \mathcal{K}}{\partial G \partial \omega} \Big|_{\text{Eq.(11)}} = \frac{\partial^2 \mathcal{K}}{\partial \omega \partial G} \Big|_{\text{Eq.(11)}} = 0. \end{array} \right. \quad (12)$$

In the equations (12), the term  $\frac{\partial^2 \mathcal{K}}{\partial \omega^2} \Big|_{\text{Eq.(11)}}$  is always strictly positive (if  $G < 1$ ). Then the equilibrium is a stable point if

$$\gamma > \frac{1}{G^5} \left( 15 \frac{H^2}{G^2} - 2 \right) \iff G_{hor}^5 > \frac{1}{7\gamma}.$$

Using this equation at the equilibrium (11), we obtain conditions for stability of the stable point ( $G \neq 1 \Leftrightarrow e \neq 0$ )

$$\left\{ \begin{array}{l} \frac{1 - 2\gamma}{5} < H^2 < \frac{1}{7} \left( \frac{1}{7\gamma} \right)^{2/5} \\ \text{and } \frac{1}{7} \leq \gamma. \end{array} \right. \quad (13)$$

So the condition to have an unstable equilibrium is given by

$$\gamma < \frac{1}{7} \quad \text{or} \quad H^2 < \frac{1-2\gamma}{5} \quad \text{or} \quad H^2 > \frac{1}{7} \left( \frac{1}{7\gamma} \right)^{2/5}. \quad (14)$$

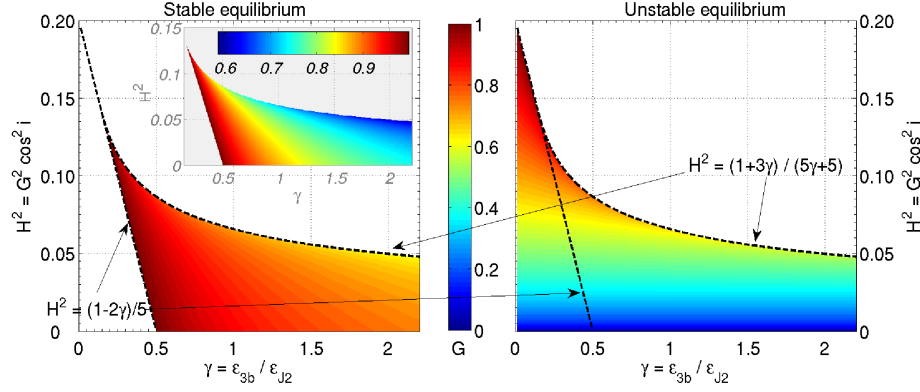


**Fig. 5** Value of  $G$  at stable (on the left) (Eqs. 12 and condition 13) equilibrium and unstable (on the right) (Eqs. 12 and condition 14) equilibrium, computed as a function of  $H^2$  and  $\gamma$ . The color code indicates the value of  $G$  at the equilibrium (horizontal equilibria:  $\omega = 0, \pi$ ). The inset on the left panel shows the same plot of left panel but using a wider color code.

In the Figure 5, we notice that when both unstable and stable equilibrium exist, the unstable equilibrium always appears for a value of  $G$  lower than that of the stable point (i.e. for a value of  $e$  greater than the one for the stable point).

## 5.2 Circular case $G = 1$ (eccentricity $e = 0$ )

For the case  $G = 1$ , we can use a canonical transformation to cartesian coordinates

$$x = \sqrt{1 - G^2} \sin \omega \quad y = \sqrt{1 - G^2} \cos \omega \quad (15)$$

The new Hamiltonian is therefore

$$\begin{aligned} \mathcal{K} = & \frac{1}{4} \left( \frac{1}{(1 - x^2 - y^2)^{3/2}} - \frac{3H^2}{(1 - x^2 - y^2)^{5/2}} \right) \\ & + \frac{3\gamma}{8} \left[ 5x^2 \left( 1 - \frac{H^2}{1 - x^2 - y^2} \right) - H^2 - 2x^2 - 2y^2 \right] \end{aligned} \quad (16)$$

for which it is obvious that  $(0, 0)$  is always an equilibrium point whose stability can be studied computing the second derivatives and evaluate them at this equilibrium:

$$\begin{cases} \frac{\partial^2 \mathcal{K}}{\partial x^2} \Big|_{x=0=y} = \frac{3}{4}(1-5H^2) + \frac{3\gamma}{4}(3-5H^2) \\ \frac{\partial^2 \mathcal{K}}{\partial y^2} \Big|_{x=0=y} = \frac{3}{4}(1-5H^2) - \frac{3\gamma}{2} \\ \frac{\partial^2 \mathcal{K}}{\partial x \partial y} \Big|_{x=0=y} = \frac{\partial^2 \mathcal{K}}{\partial y \partial x} \Big|_{x=0=y} = 0. \end{cases}$$

So, the condition to have a stability point at  $x = 0 = y$  is

$$H^2 < \frac{1-2\gamma}{5} \quad \text{or} \quad H^2 > \frac{1+3\gamma}{5\gamma+5}; \quad (17)$$

and thus the condition to have an unstable point at  $x = 0 = y$  is

$$\frac{1-2\gamma}{5} < H^2 < \frac{1+3\gamma}{5\gamma+5}. \quad (18)$$

### 5.3 Summary of the phase space

In this section we summarize the various possible phase spaces topologies as a function of the parameters. We draw (Fig. 6) the bifurcation lines (conditions 8, 13 and 17) in the parameter space  $(\gamma, H^2)$ . This bifurcation diagram is equivalent to the upper part of the bifurcation diagram in San-Juan et al (2006) but here we draw the bifurcation lines in the general (not linked to a particular central body) space  $(\gamma, H^2)$ . The  $H^2 = (7\gamma)^{-2/5}/7$  line stops at the limit  $\gamma = 1/7$ . For this value, this curve coincides with the  $H^2 = (1-2\gamma)/5$  condition. For the Jupiter-Europa-orbiter system, the minimum value of  $\gamma$  is 1.153 (Tab. 1). Therefore the phase spaces (A) and (E') do not exist.

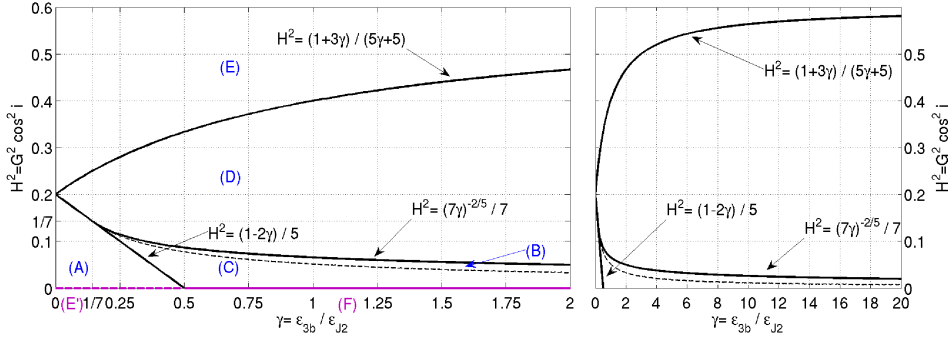


**Fig. 6** Bifurcation lines and regions in the parameter space  $(\gamma, H^2)$ . In the regions (B) and (C) we have the same number and the same stability of the equilibria but the phase space is topologically different. These regions are separated by the dashed line implicitly given by equation (19).

The region (E') and (F) in magenta color correspond to exact polar orbits ( $i = 90^\circ$  thus  $H^2 = 0$ ).

For each region, we attribute a letter and we draw (Fig. 7) a generic contour plot of the Hamiltonian (3) in the  $(k, h, \iota)$  physical space. We recall that the motion of the inclination  $\iota$  is given by the conservation of the first integral  $H = G \cos \iota$ . We also draw the projection of these phase spaces in the semi-equinoctial elements space  $(k, h) = (\sqrt{1 - G^2} \cos \omega, \sqrt{1 - G^2} \sin \omega)$ . In this phase space, it is easier to bring to the fore the stable (green point) and unstable (red cross) equilibria. The (E') phase space is trivial, containing only concentric circle in the  $\iota = 90^\circ$  plane, so we do not reproduce it.

In the Figure (7), we notice that the maximum inclination is always reached at  $e = 0$ . This is explained by the relation  $H^2 = \sqrt{1 - e^2} \cos \iota$ . This last relation also gives a maximum bound onto the eccentricity:  $e \leq \sqrt{1 - H^2}$ . Therefore there are some values of  $H$  for which the phase space is visibly restricted in eccentricity. Beyond this eccentricity, the motion is physically impossible.

Let us observe that the region near the stable equilibria allows to control the variation of the eccentricity even for high eccentricity. We also remark that there are “dangerous” portions of phase space such as the region around the  $\gamma = H^2 = 1/7$  or near of the (B)-(C) transition. In these regions the dynamics (in a full model) could change strongly for a small variation of  $(H^2, \gamma)$  or  $(e, \omega)$ .

The transition between (B) and (C) phase spaces arises when the energy of the separatrix at the  $(0, 0)$  equilibrium is equal to the energy of the unstable exterior horizontal equilibrium. This condition gives a new “fictitious” bifurcation line (dashed line in Figure 6) in the parameter space  $(\gamma, H^2)$ . To find this line, we evaluate the Hamiltonian (3) at the unstable equilibrium  $H^2 = \frac{G^2}{5}(1 - 2G^5\gamma)$  (Eq.11 and condition 14) and we denote this value by  $\mathcal{K}_1$ . Afterward, we evaluate the Hamiltonian (16) at the unstable equilibrium  $(0, 0)$  (condition 18) and denote the result by  $\mathcal{K}_2$ . We now assume these two equilibria have the same value of Hamiltonian  $\mathcal{K}$  and of  $H^2$ . Then we can replace  $H^2$  by  $\frac{G^2}{5}(1 - 2G^5\gamma)$  in  $\mathcal{K}_2$  and we impose the equality between  $\mathcal{K}_1$  and  $\mathcal{K}_2$ . Therefore we obtain the condition

$$\gamma = \frac{2 + 5G_{hor}^3 + 3G_{hor}^5}{6G_{hor}^{10} + 15G_{hor}^3 - 21G_{hor}^5} \quad \text{where } H^2 = \frac{G_{hor}^2}{5}(1 - 2G_{hor}^5\gamma) \quad (19)$$

where  $G_{hor}$  is the unstable horizontal equilibrium i.e.  $H^2 = \frac{G_{hor}^2}{5}(1 - 2G_{hor}^5\gamma)$ . We plot this implicit condition (19) in Figure 6 with a dashed black line. This line joins the “ $(1 - 2\gamma)/5$ ” and “ $(7\gamma)^{-2/5}/7$ ” lines at the  $(\gamma = 1/7, H^2 = 1/7)$  point.

For the particular case  $\gamma \rightarrow 0$  ( $J_2$  effect only), we obtain, for all  $H^2$ , a phase space with circular motion of the eccentricity. We see that near to the value  $H^2 = 1/2$  (corresponding to the Molniya<sup>1</sup> critical inclination equal to  $63.43^\circ$  with  $G = 1$ ), the phase spaces (A), (D) and (E) always exist until  $\gamma$  becomes exactly equal to 0. In the opposite case,  $\gamma \rightarrow \infty$  (third body effect only), the curve  $H^2 = (7\gamma)^{-2/5}/7$  converges to 0 and the curve  $H^2 = (1 + 3\gamma)/(5\gamma + 5)$  converges to  $3/5$  (corresponding to the Kozai-Lidov critical inclination equal to  $39.23^\circ$  with  $G = 1$ ). Then only the following phase spaces are realizable: (E) (for  $H^2 > 3/5$ ), (D) (for  $0 < H^2 < 3/5$ ) and (F) (for  $H^2 = 0$ ) with (F) that degenerates to an unstable point at the center. These three phase spaces will be shown in Figure 12.

<sup>1</sup> At this inclination, due to  $J_2$  effect, the argument of perigee remains nearly constant for a long period of time. Molniya orbits are named after a series of Soviet/Russian Molniya communications satellites which have been using this type of orbit since the mid 1960s.

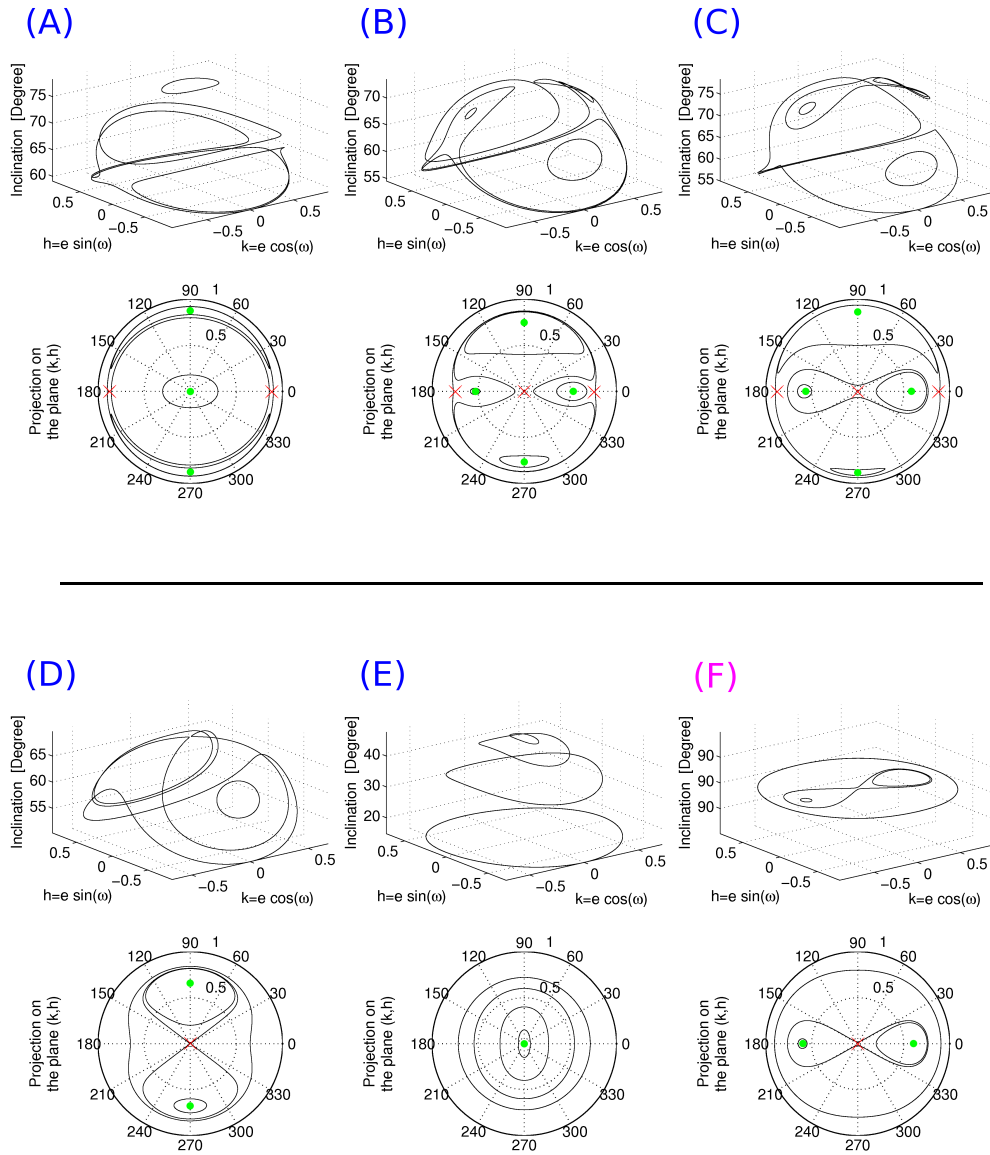


**Fig. 7** Examples of some generic contour plots of the Hamiltonian (3) in  $(k, h, i)$  space for each region of Fig. 6. The inclination  $i$  is given in degrees and the semi-equinoctial elements  $(k, h)$  are given by  $(k, h) = (\sqrt{1 - G^2} \cos \omega, \sqrt{1 - G^2} \sin \omega)$ . The green point and red cross are respectively the stable and unstable points. In the polar projection, the radius is the eccentricity  $e$  and the angle is the pericenter  $\omega$  in degrees.

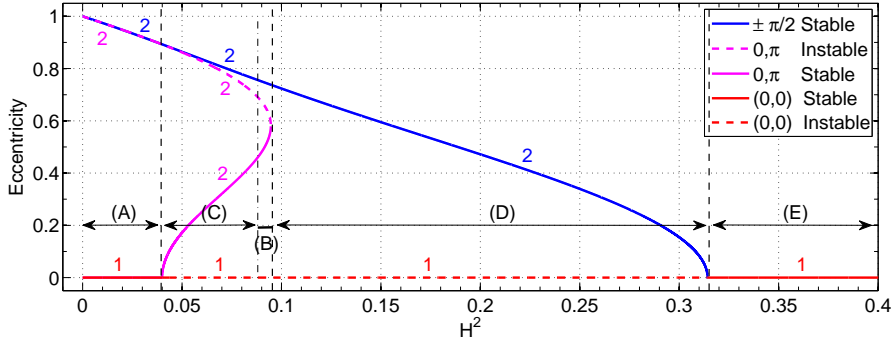


**Fig. 8** For a vertical section ( $\gamma = 0.4$ ) in the Figure 6, value of the eccentricity at unstable (dashed color lines) and stable (solid color lines) equilibria with respect to  $H^2$ . The numbers give the number of equilibria for each curve.

In Figure 8, we show how the stable and unstable equilibria evolve, appear and disappear in each region and during the transition between the regions. We take a vertical section in the Figure 6 at  $\gamma = 0.4$ . This section crosses the regions (A), (C), (B), (D) and (E). We draw the value of the eccentricity at the stable (solid color lines) and unstable (dashed color lines) equilibria with respect to  $H^2$ . The vertical dashed black lines mark the boundary of the regions. The numbers give the number of equilibria with this value of  $e$ . For example, 2 in magenta dashed line means that there are two unstable equilibria with the same value of  $e$ , respectively for  $\omega = 0$  and  $\omega = \pi$ .

At the transition between (A) and (C), the central ( $e = 0$ ) stable point bifurcates in two horizontal stable points ( $e \neq 0$  and  $\omega = 0, \pi$ ) and one unstable point ( $e = 0$ ). At the transition between (B) and (D), the two unstable and the two stable horizontal ( $\omega = 0, \pi$ ) equilibria converge to the same value of  $e$  and cancel out. At the transition between (D) and (E), the two stable Kozai-Lidov equilibria ( $\omega = \pm\pi/2$ ) come close to 0 and cancel out with the central unstable equilibrium to give one central stable equilibrium. We remark that the transition between (C) and (B) is not characterized by a change of the equilibria.

#### 5.4 Period at the equilibrium

We are now interested in the period of the eccentricity vector at the equilibrium. This will be done by linearizing in a neighborhood of the equilibrium. Then the Hamiltonian close to the equilibrium is given by (the subscript  $eq.$  means “evaluated at the

equilibrium”):

$$\begin{aligned} \mathcal{K} &= \mathcal{K}_{eq.} + \underbrace{\frac{\partial \mathcal{K}}{\partial G} \Big|_{eq.}}_{=0} (G - G_{eq.}) + \underbrace{\frac{\partial \mathcal{K}}{\partial \omega} \Big|_{eq.}}_{=0} (\omega - \omega_{eq.}) \\ &+ \underbrace{\frac{1}{2} \frac{\partial^2 \mathcal{K}}{\partial G^2} \Big|_{eq.}}_{\substack{\text{not } a \\ \underline{a}}} (G - G_{eq.})^2 + \underbrace{\frac{\partial^2 \mathcal{K}}{\partial G \partial \omega} \Big|_{eq.}}_{=0} (G - G_{eq.})(\omega - \omega_{eq.}) + \underbrace{\frac{1}{2} \frac{\partial^2 \mathcal{K}}{\partial \omega^2} \Big|_{eq.}}_{\substack{\text{not } b \\ \underline{b}}} (\omega - \omega_{eq.})^2 \end{aligned}$$

$$\mathcal{K} = \mathcal{K}_{eq.} + aX^2 + bY^2 .$$

This is an harmonic oscillator that can be expressed in action-angle variables  $(\psi, J)$  defined as (at a stable equilibrium, we have  $ab > 0$ ):

$$X = \sqrt[4]{\frac{b}{a}} \sqrt{2J} \cos \psi \quad \text{and} \quad Y = \sqrt[4]{\frac{a}{b}} \sqrt{2J} \sin \psi .$$

Then the frequency at the equilibrium is given by

$$\dot{\psi} = \frac{\partial \mathcal{K}}{\partial J} = 2\sqrt{ab} = \sqrt{\frac{\partial^2 \mathcal{K}}{\partial G^2} \Big|_{eq.} \frac{\partial^2 \mathcal{K}}{\partial \omega^2} \Big|_{eq.}} . \quad (20)$$

Using the equation (20), the periods ( $\tau$ ) at the stable equilibria are given by:

- for horizontal equilibria:  $G$  such as Equation (11) and condition of stability (13)

$$\tau = \frac{4\pi}{3\sqrt{\frac{5}{2} \left[ \frac{\varepsilon_{J_2}}{G^5} \left( 2 - 15 \frac{H^2}{G^2} \right) + \varepsilon_{3b} \right] \varepsilon_{3b} (1 - G^2) \left( 1 - \frac{H^2}{G^2} \right)}} ;$$

- for vertical (Kozai-Lidov) equilibria:  $G$  such as Equation (7) and condition of stability (8)

$$\tau = \frac{4\pi}{3\sqrt{-\frac{5}{2} \left[ \frac{\varepsilon_{J_2}}{G^5} \left( 2 - 15 \frac{H^2}{G^2} \right) - \frac{3\varepsilon_{3b}}{2} \left( 1 + 5 \frac{H^2}{G^4} \right) \right] \varepsilon_{3b} (1 - G^2) \left( 1 - \frac{H^2}{G^2} \right)}} ;$$

- for central equilibrium ( $e = 0$ ):  $G = 1$  with condition of stability (17)

$$\tau = \frac{8\pi}{3\sqrt{\left[ \varepsilon_{J_2} (1 - 5H^2) + \varepsilon_{3b} (3 - 5H^2) \right] \left[ \varepsilon_{J_2} (1 - 5H^2) - 2\varepsilon_{3b} \right]}} .$$

We remind that  $\gamma = \varepsilon_{3b}/\varepsilon_{J_2}$  and that the equations are dimensionless. Then the periods at the equilibria are given by  $T_{eq.} = \sqrt{\frac{a^3}{GM}} \tau_{eq.}$ .

For example, we apply these formula to a Mercury orbiter. The values for Mercury are  $a_{3b} = 57\,909\,176.0$  km,  $e_{3b} = 0.205\,630\,69$ ,  $J_2 = 6.0 \times 10^{-5}$  (Anderson et al 1987) and  $R_p = 2\,439.99$  km. In the Figure 9 we plot the periods at the equilibria respectively for the three cases:

- on the left panel, the periods at the stable equilibrium with respect to the value of  $\gamma$  and  $H^2$ . The color code indicates the period of the fundamental frequency at the equilibrium;
- on the right panel, the location of the stable equilibrium in the phase space  $(a, e, i)$  with the period in the color scale.

The color code is the same for the left and right panels and it is truncated at the value of 100 years. For a larger period, we use the black color.



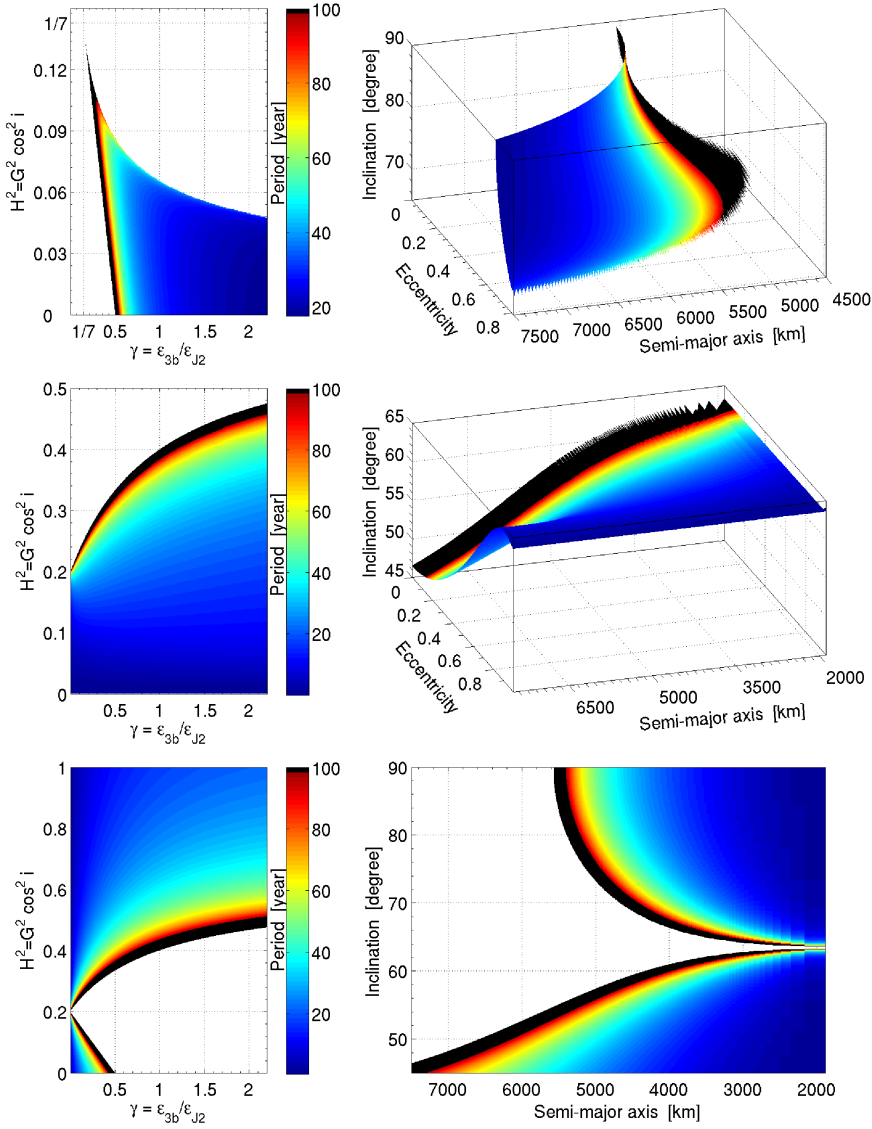


**Fig. 9** Plot of the periods at the stable horizontal equilibrium (Eq. 11 with conditions 13), vertical equilibrium (Eq. 7 with condition 8) and  $(0, 0)$  equilibrium (with conditions 17) respectively in the upper, center and lower panels. The color code indicates the period (truncated to 100 years) of the fundamental frequency at the equilibrium. On the left panels, the period with respect to the parameters  $(\gamma, H^2)$ . On the right panels, the location of the stable equilibrium in the physical space  $(a, e, i)$  with its period. For the equilibrium  $(0, 0)$ ,  $e$  is always equal to 0.

## 6 Comparison of analytical and numerical solutions

### 6.1 Comparison for all inclinations

The analytical results of the simplified model described above are checked using a precise numerical integration of the complete set of equations of motion (1). For our test, we use Mercury's orbiter mission profile, which nominally puts the spacecraft into a high eccentric polar orbit. Numerical integrations were performed with the Bulirsch-Stoer (Stoer and Bulirsch 1980) integrator. We reproduce hereby a few characteristic plots of the numerical simulations to confirm our analytical theory (see Figure 10). Similar results have been obtained for a wide range of initial frozen orbit conditions.

Figure 10 shows a very good agreement between analytical results and numerical simulations.

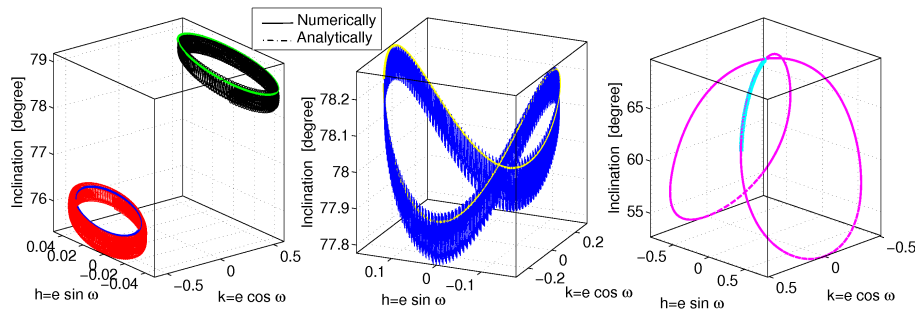


**Fig. 10** Comparison between analytical and numerical results. For the left and right panel, the initial conditions are  $a_0 = 6407$  km ( $\gamma = 1.000296$ ),  $\Omega_0 = M_0 = 0^\circ$ . In the left panel, for the lower orbit, we take  $e_0 = 0.545055$  ( $G = 0.8384$ ),  $\iota_0 = 76.646989^\circ$  ( $H^2 = 3.7492 \times 10^{-2}$ ) and  $\omega_0 = 180^\circ$ ; for the upper orbit, we take  $e_0 = 0.6$  ( $G = 0.8$ ),  $\iota_0 = 78.221768^\circ$  ( $H^2 = 0.26666666$ ) and  $\omega_0 = 0^\circ$ . For the right panel, the initial conditions are  $e_0 = 0.01$  ( $G = 0.99995$ ),  $\iota_0 = 69.73104^\circ$  ( $H^2 = 0.1199999$ ) and  $\omega_0 = 0^\circ$ . For the middle panel, the initial conditions are  $a_0 = 4650$  km ( $\gamma = 0.17096$ ),  $e_0 = 0.3$  ( $G = 0.9539392$ ),  $\iota_0 = 77.89775^\circ$  ( $H^2 = 0.04$ ) and  $\Omega_0 = M_0 = \omega_0 = 0^\circ$ . The numerical model takes into account the contribution of  $J_2$  and  $C_{22}$  and the solar gravitational effect, with starting epoch fixed at 14 September 2019. The analytical model is based on Equations (4, 5, 6). We plot the numerical integrations with continued lines and the analytical results with dashed lines. In the right panel, the numerical integration leads to a crash onto the planet.

### 6.2 Comparison for polar inclination and explanation of the preliminary numerical results

In the Figure 11, we present a graphical comparison between numerical integration and analytical results (contour plots of the Hamiltonian (3)) for an exact polar inclination. We see that the analytical theory is very close to the numerical integration for all initial eccentricities. We also notice that the addition of the  $C_{22}$  does not modify much the motion.

In the right panel, we show two solutions close to the libration point and we see that, the closer the motion is to the libration equilibrium, the more the numerical

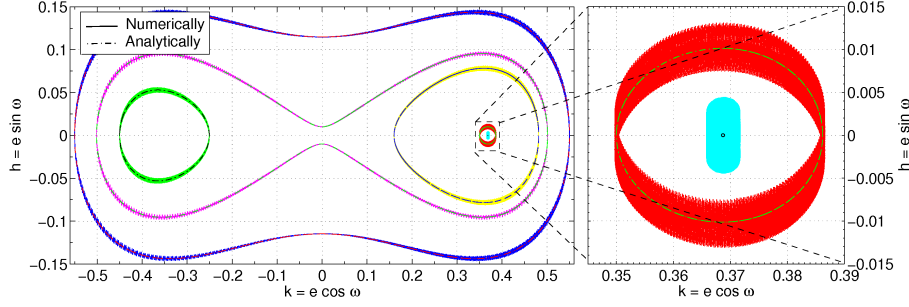


**Fig. 11** Comparison between analytical and numerical results for exact polar orbiter. The initial conditions are  $a_0 = 6000$  km ( $\gamma \simeq 0.72$ ),  $i_0 = 90^\circ$ ,  $\Omega_0 = 67.7^\circ$ ,  $\omega_0 = -2^\circ$ ,  $M = 36.4^\circ$ . The numerical and analytical model are the same of Figure 10. In dashed line the analytical result and in continued line the numerical integration. On the right a blow-up of the center of libration.

integrations show a discrepancy with respect to the analytical results for the periherm libration: the frozen orbit of the analytical model shows no changes in eccentricity and argument of pericenter. On the contrary, the numerical orbit has short period oscillations but constant mean values of  $e$  and  $\omega$ .

Figure 11 allows us to explain the behaviors already seen in our preliminary numerical exploration (Fig. 1). In fact we can find there different orbits with a semi-major axis equal to 6000 km corresponding to a vertical section in Figure 1. Then, on this section, we take some values of the eccentricity such that:

- for  $e$  near to 0, in Fig. 1, we see a large value of the amplitude of variation of the eccentricity approximately equal to 0.5 and a high value of the second derivative. In Fig. 11, for  $e$  equal to 0, we are on the separatrix. Therefore the eccentricity increases (roughly until 0.5) and a little shift of the initial eccentricity causes a high difference of the frequency. Thus the second derivative of the frequency is large;
- for  $e$  close to 0.37, in Fig. 1, we see that the amplitude of variation of the eccentricity decreases until 0. In Fig. 11, at  $e = 0.37$ , we find the stable point where the eccentricity is equal to a constant;
- when  $e$  moves away from 0.37 to 0.5, in Fig. 1, we see that the amplitude of variation of the eccentricity increases from 0 to 0.5 and for  $e = 0.5$ , the amplitude of variation of the eccentricity is maximal and the value of the second derivative is large. In Fig. 11, moving away from the equilibrium ( $e = 0.37$ ) toward the separatrix ( $e \simeq 0.5$ ) we encounter larger and larger variations in  $e$ ;
- for  $e$  near to 0.58, in Fig. 1, we see that the amplitude of variation of the eccentricity is smaller than for  $e \simeq 0.5$ . In Fig. 11, for  $e \simeq 0.58$ , the pericenter circulates and the maximum of the amplitude of variation of the eccentricity is roughly equal to  $0.58 - 0.12 = 0.46$ .
- in Fig. 1, moving along the line  $e = 0$ , we pass from the region (F) to the region (E') at 5577 km (Tab.1). For semi-major axis smaller than  $a = 5577$  km, we do not cross any separatrix and the amplitude of variation of the eccentricity is small.

**Table 2** Comparison between the period of the equilibria determined in the analytical model and the period numerically obtained using NAFF.

Initial condition				Period [year]		Error
What Equi.	$a$ [km]	$e$	$i$ [degree]	Analytical	Numerical	relative %
Kozai	5 750	0.4731	58.37	29.30	29.25	0.17
Horiz.	8 083	0.4922	77.68	35.67	35.61	0.17
Horiz.	5 818	0.5418	71.93	42.17	42.26	0.21
(0,0)	3 429	0.0	47.64	9.127	9.135	0.08
(0,0)	4 731	0.0	77.01	56.594	55.274	2.38

### 6.3 Frequency comparison

To obtain a second independent validation of our analytical model, we numerically compute, using the NAFF algorithm (Laskar 1988, 2005), the period of the numerical solutions of the full system (1) obtained through numerical integration, and we compare it with the period of the equilibrium points of the simplified model.

Table 2 provides a summary of this comparisons. We can observe a very good agreement between the two methods. Some small differences can be explained as follows:

- the exact equilibrium in the doubly averaged system is not the exact equilibrium in the full numerical model;
- the full numerical model contains short period terms which disturb the long period dynamics.

## 7 Discussions

### 7.1 $J_2$ : the protector

The aim of this section is to describe the protection mechanism of the coefficient  $J_2$  on the increase of the eccentricity. We recall that our Hamiltonian (3), once we set the coefficient  $\varepsilon_{j_2} = 0$ , reduces to the Kozai-Lidov Hamiltonian:

$$\mathcal{K}_{kl} = \frac{3\varepsilon_{3b}}{8} \left[ 5(1 - G^2) \left( 1 - \frac{H^2}{G^2} \right) \sin^2 \omega - H^2 - 2 + 2G^2 \right]. \quad (21)$$

In the Figure 12, we draw the possible phase spaces of this Hamiltonian. In the right panel ( $H^2 > 3/5$ ) we have a similar behavior of our (E) case (Fig. 7). For the exact polar orbits ( $H^2 = 0$  in the left panel of the Fig. 12), in the Kozai-Lidov Hamiltonian, all the probes are ejected: the eccentricity always grows up to 1. Instead, with the addition of the coefficient  $J_2$  we have the phase space (E') or (F) (Fig. 7) where it is possible that the eccentricity does not increase or that it remains at a fixed value. In the middle case ( $0 < H^2 < 3/5$ ) we see that for an initial pericenter close to 0, the eccentricity increases. Instead, in our case, the phase spaces (A), (B), (C) and (E) (Fig. 7) show that it is possible to find initial condition (other than  $\omega \simeq \pm\pi/2$ ) where the increasing of the eccentricity is naturally controlled.

The  $J_2$  acts as a protection mechanism against the increase of the eccentricity due to the Kozai-Lidov effect. This mechanism also appears for planets in tight binary systems (Saleh and F.A. 2009), where the general relativistic effects become dominant and can cause the periastron to precess on very short timescales. Therefore this precession can lead to the suppression of Kozai oscillations.

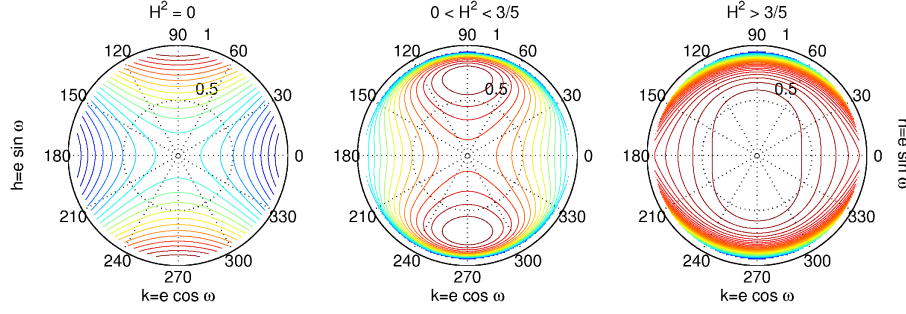


**Fig. 12** All possible phase spaces for Kozai-Lidov Hamiltonian (21) with respect to the values of  $H^2$ .

## 7.2 Local deformation of the Kozai-Lidov equilibrium

We have seen that the condition to get the Kozai-Lidov equilibrium is (Eq. 8)

$$H^2 < \frac{1 + 3\gamma}{5\gamma + 5}.$$

Actually there is a region where it is possible to find three real roots for  $G$  on a function of  $H^2$  and  $\gamma$ . The conditions to have these three real roots are given by:

$$KL_3 \equiv \begin{cases} 864\,000\,H^{16}\gamma^6 + (2\,963\,520\,H^{12} - 1\,024\,H^{10})\gamma^4 \\ \quad + (1\,512\,630\,H^8 - 13\,965\,H^6 - 22\,235\,661\,H^{10})\gamma^2 + 12 = 0 \\ \text{and } H^2 \leq \frac{1}{3087} \end{cases}$$

We draw the solutions of this equation, denoted by  $KL_3$ , that demarcates the region denoted (G), on the left panel of the Figure 13. Let us observe that this condition verified for large value of  $\gamma$  ( $\gamma \geq 7203\sqrt{3}/2$ ) and for very small value of  $H^2$  ( $H^2 \leq 1/3087$ ). An example of the phase space is plot in Figure 13 in the middle panels. In this region, the vertical Kozai-Lidov stable equilibrium bifurcates in two stable and one unstable vertical Kozai-Lidov equilibria producing thus a local deformation of the Kozai-Lidov equilibrium. We show an example of these three equilibria in the right panels of the Figure 13. Initial conditions close to these equilibria (external orbit in the right panels of Fig. 13) give rise to orbit librating around this set of three equilibria.

It is possible to find that this bifurcation appears, in the (G) region, for a value of  $G$  smaller than  $\sqrt{3}/21 \simeq 0.0824786$  corresponding to a value of the eccentricity  $e$  larger than  $\sqrt{438}/21 \simeq 0.99659$ . Recalling the formula  $H = G \cos \iota$ , we obtain a minimal inclination of  $87.27^\circ$ .

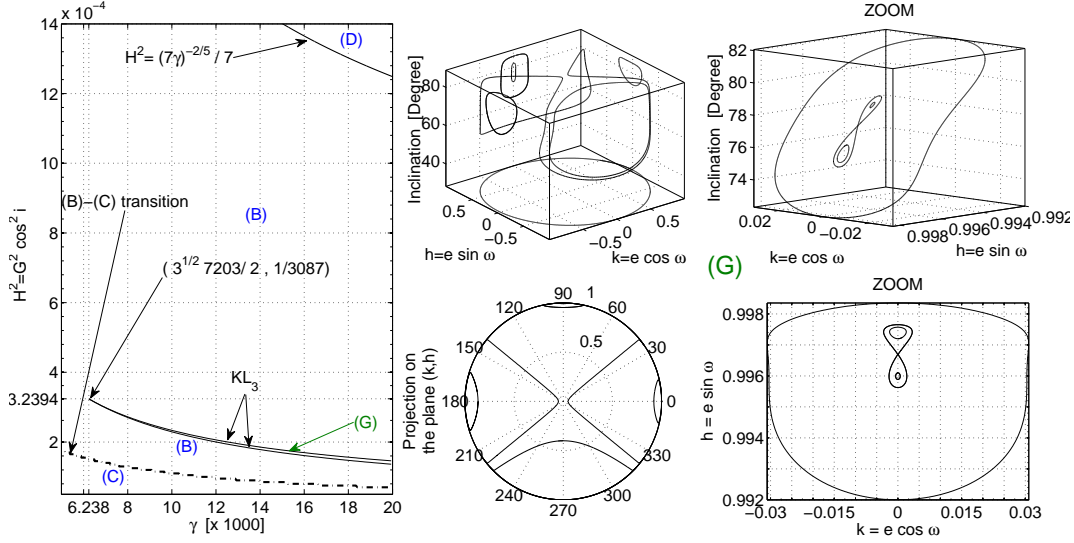


**Fig. 13** Local deformation of the Kozail-Lidov equilibrium. The bifurcation lines in the left panel with the new region (G) demarcated by the two curves  $KL_3$ . Example of generic contour (for (G) region) of the Hamiltonian (3) in  $(k, h, i)$  space in the middle panels. A zoom of the local deformation in the right panels.

### 7.3 $J_3$ discussion

In Paskowitz and Scheeres (2006) the authors included the  $J_3$  (the “pear shape” of the central body) Europa’s effect in their system. They noticed that the coefficient  $J_3$  caused an asymmetry between the solutions of the frozen orbits for  $\omega = \pm\pi/2$  but they did not explain the reasons of this behavior.

The potential arising from a central body with a  $J_3 \neq 0$  is given by

$$\Phi_{J_3}(\mathbf{r}) = \frac{GMJ_3R_p^3}{2r^7} (\mathbf{r} \cdot \mathbf{n}_p) \left[ 5(\mathbf{r} \cdot \mathbf{n}_p)^2 - 3r^2 \right].$$

The averaged Hamiltonian is then

$$\frac{3GMJ_3R_p^3}{2a^4(1-e^2)^{5/2}} e \sin \omega \sin i \left( 1 - \frac{5}{4} \sin^2 i \right).$$

Using our variables  $G = \sqrt{1-e^2}$ ,  $H = G \cos i$ , we can define the dimensionless (divided by  $GM/a$ ) potential that we can add to the Hamiltonian (3):

$$\underbrace{\frac{J_3R_p^3}{a^3}}_{\equiv \varepsilon_{J_3}} \frac{3}{8G^8} \sqrt{1-G^2} \sin \omega \sqrt{G^2-H^2} (5H^2-G^2).$$

Introducing the coefficient  $\delta = \frac{\varepsilon_{J_3}}{\varepsilon_{J_2}} = \frac{J_3 R_p}{J_2 a}$ , the equations of motion (6 and 5) can be rewritten in compact form as follows:

$$\begin{cases} \dot{G} = F_1(G, H, \gamma) \sin \omega \cos \omega + F_2(G, H, \delta) \cos \omega \\ \dot{\omega} = F_3(G, H, \gamma) + F_4(G, H, \gamma) \sin^2 \omega + F_5(G, H, \delta) \sin \omega \end{cases}$$

where the functions  $F_1$ ,  $F_3$  and  $F_4$  can be easily identified in equations (5) and (6). The functions  $F_2$  and  $F_5$  come from the  $J_3$  effect and they are proportional to  $\delta$ .

### 7.3.1 Vertical equilibria – Kozai-Lidov equilibria: $\cos \omega = 0 \Leftrightarrow \omega = \pm\pi/2$

Let us observe that the addition of  $J_3$  effect causes an asymmetry in the frozen orbit solutions not present before. Indeed, for  $\omega = \pi/2$  the condition of equilibrium is given by

$$F_3(G, H, \gamma) + F_4(G, H, \gamma) + F_5(G, H, \delta) = 0$$

whereas for  $\omega = -\pi/2$  the condition of equilibrium is given by

$$F_3(G, H, \gamma) + F_4(G, H, \gamma) - F_5(G, H, \delta) = 0.$$

Then, for a small coefficient  $\delta$ , the asymmetry is not important. However for a large value of this coefficient, the asymmetry could be important until the elimination of one of two equilibria.

### 7.3.2 Horizontal equilibria.

For horizontal equilibria, the condition of equilibrium ( $\dot{G} = 0$ ) becomes:

$$F_1(G, H, \gamma) \sin \omega + F_2(G, H, \delta) = 0 \iff \sin \omega = -F_2/F_1 \stackrel{not.}{=} -\epsilon.$$

Then the “horizontal” equilibria appear for non-zero values of the pericenter  $\omega = -\epsilon$  and  $\omega = \pi + \epsilon$ . The condition to obtain  $\dot{\omega} = 0$  becomes:

$$F_3(G, H, \gamma) + F_4(G, H, \gamma)\epsilon^2 - F_5(G, H, \delta)\epsilon = 0,$$

that induces a shift in the equilibrium in  $G$  and  $\omega$  variables with respect to the case “ $J_2$  + third body”.

### 7.3.3 Modifications of the phase space

For illustration, in Figure 14, we draw the contour plots of the new Hamiltonian for different values of  $J_3$  (or for different values of  $\delta$ ). We see that when the  $\delta$  coefficient increases (in absolute value), the vertical equilibrium goes down while the horizontal equilibrium goes below the “line  $\sin \omega = 0$ ”. We point out that, from some values of  $\delta$ , the equilibrium  $\omega = -\pi/2$  disappears (Fig. 14 right panel).

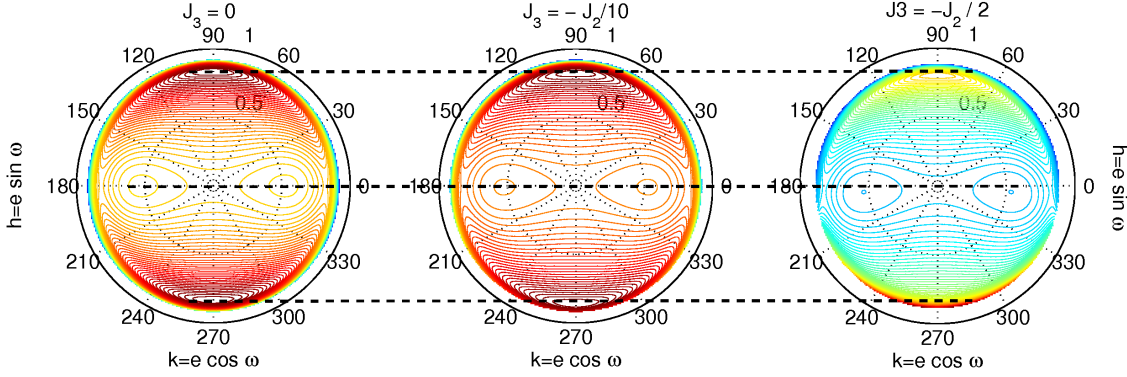


**Fig. 14** Distortion of the phase space (for a Mercury's orbiter) due to  $J_3$  effect. The initial conditions are  $a = 5\,900$  km ( $\gamma \simeq 0.66$ ) and  $H^2 = 0.06$ .  $J_3$  (respectively  $\delta$ ) is equal to 0 (0),  $-J_2/10$  ( $-0.041356$ ) and  $-J_2/2$  ( $-0.20678$ ) in left, center and right panels.

### 7.3.4 BepiColombo and other missions

At present time, the semi-major axis of the two orbiters (MPO & MMO) of the Bepi-Colombo mission are respectively equal to 3 394 km and 8 552 km. The MPO altitude corresponds to our (E') phase space where the eccentricity vector has a circular concentric motion. The MMO initial conditions, without thrust correction, leads to a crash onto the Mercury surface after 3 years. Thanks to our theory, we can choose another initial condition  $a = 7\,355$  km and  $e = 0.652$ , that avoids the crash on Mercury and whose eccentricity vector is fixed.

## 8 Conclusions

The orbit dynamics of a space probe orbiting a planet or a natural planetary satellite has been investigated. The proposed model includes the effects of  $J_2$  for the central body and the perturbation of the third body. We have developed a doubly averaged Hamiltonian and studied the location of the stable and unstable frozen orbits. Our analytical approach allows us to compute also the periods of the free librations at the equilibria. The analytical results have been checked and validated numerically by performing numerical integrations of the complete systems. Our theory is able to explain the behavior of our preliminary numerical investigations where the variation of the amplitude of the eccentricity is null and the presence of a separatrix has been found by numerical investigation. The theory is general enough to be applied to a wide range of probes around any planet or any natural planetary satellite, provided that they respect the hypotheses used to obtain our Hamiltonian model.

We have shown the protection mechanism of the coefficient  $J_2$  on the increasing of the eccentricity due to Kozai-Lidov effect. This mechanism is therefore able to find a larger number of frozen orbits than for the only Kozai-Lidov problem. We have also explained the asymmetry of the frozen equilibria caused by the addition of the



coefficient  $J_3$ . We have also brought to the light a local deformation of the Kozai-Lidov equilibria that appears at high eccentricity, high inclination and large value of  $\gamma$ .

It would be interesting to take this theory into account to choose the initial semi-major axis and eccentricity of an orbiter for future missions around planets or planetary satellites.

**Acknowledgements** The authors thank B. Noyelles and A. Albouy for fruitful discussions, the IMCCE team for their welcome and B. Meyssignac for initializing discussion.

Numerical simulations were made on the local computing resources (*Cluster URBM-SYSDYN*) at the University of Namur (FUNDP, Belgium).

This work was partly supported by the fellowship *Concours des bourses de voyage de la Communauté Française de Belgique* obtained by Nicolas Delsate.

## References

- Anderson J, Colombo G, Esposito P, Lau E, Trager G (1987) The mass, gravity field, and ephemeris of mercury. *Icarus* Vol.71:pp.337–349
- Brouwer D, Clemence G (1961) *Methods of Celestial Mechanics*. Academic Press
- Garcia D, de Pascale P, Jehn R (2007) Bepicolombo mercury cornerstone consolidated report on mission analysis. Tech. rep., MAO Working Paper No. 466, ESOC
- Hairer E, Norsett S, Wanner G (1993) *Solving ordinary differential equations I. Nonstiff problems*. 2nd edition. Springer-Verlag
- Kozai Y (1962) Secular perturbations of asteroids with high inclination and eccentricity. *Astronomical Journal* Vol.67:pp.591
- Laskar J (1988) Secular evolution of the solar system over 10 million years. *Astronomy and Astrophysics* 198:pp.341–362
- Laskar J (2005) Hamiltonian systems and fourier analysis: new prospects for gravitational dynamics, *Advances in Astronomy and Astrophysics*, chap Frequency map analysis and quasiperiodic decomposition, pp 99–129
- Lemaître A, Delsate N, Valk S (2009) A web of secondary resonances for large A/m geostationary debris. *Celestial Mechanics and Dynamical Astronomy* Vol.104:pp.383–402
- Lidov ML (1963) Evolution of the orbits of artificial satellites of planets as affected by gravitational perturbation from external bodies. *AIAA Journal* p pp.1985
- Paskowitz M, Scheeres D (2004) Orbit mechanics about planetary satellites. *American Astronautical Society* Vol.244
- Paskowitz M, Scheeres D (2006) Design of science orbits about planetary satellites: Application to europa. *Journal of Guidance, Control and Dynamics* Vol.29
- Saleh L, FA R (2009) The stability and dynamics of planets in tight binary systems. *The Astrophysical Journal* Vol.694:pp.1566–1576
- San-Juan J, Lara M, Ferrer S (2006) Phase space structure around oblate planetary satellites. *Journal of Guidance, Control, and Dynamics* Vol.29
- Scheeres D, Guman M, Villac B (2001) Stability analysis of planetary satellite orbiters: Application to the europa orbiter. *Journal of Guidance, Control and Dynamics* Vol.24
- Standish EM (1998) JPL planetary and lunar ephemeris, de405/le405. JPL Interoffice Memorandum IOM 312.D-98-048
- Stoer J, Bulirsch R (1980) *Introduction to numerical analysis*. Springer-Verlag, New York

Sturm C (1835) Mémoire présentés par divers saavnts à l'Académie royale des SCiences de l'Institut de France, vol Vol.6, chap Mémoire sur la résolution des équations numériques

Tremaine S, Touma J, Namouni F (2009) Satellite dynamics on the laplace surface. The astronomical journal Vol.1137:pp.3706–3717

**Appendix:** “*Le théorème d’algèbre de Sturm*”

Let  $f(x)$  be a polynomial of positive degree with real coefficients and let  $\{f_0(x), f_1(x), f_2(x), \dots, f_s(x)\}$  be the standard sequence for  $f(x)$  such as

$$\begin{aligned} f_0(x) &= f(x) \\ f_1(x) &= f'(x) \\ f_2(x) &= q_0(x)f_1(x) - f_0(x), & \deg f_2 < \deg f_1 \\ f_3(x) &= q_1(x)f_2(x) - f_1(x), & \deg f_3 < \deg f_2 \\ &\dots \\ f_{i+1}(x) &= q_{i-1}(x)f_i(x) - f_{i-1}(x), & \deg f_{i+1} < \deg f_i \\ &\dots \\ &\text{until } f_{s+1}(x) = 0 \end{aligned}$$

where  $f_{i-1}$  is obtained by the Euclidean division:  $f_{i+1} = q_{i-1}f_i - f_{i-1}$ . Assume  $[a, b]$  is an interval such that  $f(a) \neq 0 \neq f(b)$ . Then the number of distinct roots of  $f(x)$  in  $[a, b]$  is  $V_a - V_b$  where  $V_c$  denotes the number of variations in sign of  $\{f_0(c), f_1(c), \dots, f_s(c)\}$ . The 0 are dropped from the sequence.